ADVANCED ENGINEERING MATERIALS
www.aem-journal.com

Densification and Strengthening of Ferrous-Based Powder Compacts Through Cold Sintering Aided Warm Compaction

Linsea Paradis, Daudi Waryoba, Kyle Robertson, Arnaud Ndayishimiye, Zhongming Fan, Ramakrishnan Rajagopalan, and Clive A. Randall*

Cold sintering of surface-modified iron compacts results in a co-continuous phosphate interphase between iron particles that provide both enhanced green strength and green density similar to the process that has been successfully introduced in low-temperature densification of ceramic materials. Relative density as high as 95% along with transverse rupture strength of ≈ 75 MPa, which is almost six times that of conventional powdered metal iron compact and 2.5 times that of warm compacted controls, is achieved. Dilatometry study at different pressures shows a small but significant improvement in densification process during cold sintering relative to the larger densification of warm compacted control. Strength model based on microstructural analysis as well as in situ diffused reflectance infrared Fourier transform spectroscopy (DRIFTS) experiments reveals the nature of the interphase that imparts the large cohesive strength under the cold sintered assisted warm compaction. The process is conducive to produce iron compacts for green machining. Furthermore, the samples when subjected to high-temperature sintering yield a fully sintered iron compact with density $> 7.2\ \mathrm{g\,cm^{-3}}$ and transverse rupture strength as high as 780 MPa. All in all, there are major new opportunities with the cold sintered assisted warm compaction of powdered metals that will also be discussed.

1. Introduction

Powdered metal processing is a well-established manufacturing technology that utilizes optimum amount of energy and materials to transform a pressed powdered metal of desired net shape to a sintered metal component. Green strength is an important property that determines the production rate and allows the handling of the parts prior to conventional high-temperature sintering that is usually performed at several hundred or thousand degree Celsius. Higher green strength is also paramount for green machining in P/M processes which can significantly improve tool life and ability to make complex parts using sinter-hardenable materials. However, this requires the green strength of powdered compacts to be greater than 20–30 MPa, which is at least twice that of conventional P/M compacts.[1] Additionally, P/M manufacturing of soft magnetic composites are gaining prominence and the ability to produce highly dense green or partially sintered iron compacts with insulating boundaries and enhanced mechanical strength can potentially open new P/M processing route for manufacture of components for electrical motor segments.

Green strength and green density of P/M compacts are largely impacted by three powder variables that include geometric factors such as particle size and shape; surface area and roughness; and intrinsic factors such as impurities or oxide layer and surface-related features such as adsorbed species and lubricants.[2] It has also been shown that the use of lubricants from classes of silanes, titanates, aluminates, and zirconates can result in an insulating inorganic coating on iron powders that can yield 95% relative density at a compaction pressure above 800 MPa.[3] Surface treatment has also shown improvement in the green strength. Several groups have shown that copper-coated iron powders can improve the green strength.[4] Improved surface roughness for mechanical interlocking and cold welding has been considered as the dominant mechanism to increase the green strength.[5] Increase in green strength has also been accomplished using special polymeric lubricants.[6] The higher strength due to the addition of polymeric lubricants is attributed to their better intrinsic mechanical properties as compared to conventional metallic stearates or ethylene bis stearamide (EBS) wax lubricants. In particular, strong intermolecular interactions that are aided by either acid base interactions or strong polar groups with sufficiently high molecular weight favor

L. Paradis, C. A. Randall
Department of Materials Science and Engineering
The Pennsylvania State University
University Park, PA 16802, USA

D. Waryoba, K. Robertson, R. Rajagopalan
Department of Engineering
Penn State DuBois
DuBois, PA 15801, USA
E-mail: rur12@psu.edu

A. Ndayishimiye, Z. Fan, R. Rajagopalan, C. A. Randall
Materials Research Institute
University Park, PA 16802, USA

The ORCID identification number(s) for the author(s) of this article can be found under https://doi.org/10.1002/adem.202200714.

DOI: 10.1002/adem.202200714

the formation of a thin and strong film that adheres to the metal particles and strengthens the green compact.

From a process point of view, warm compaction and warm die compaction are two industrially viable routes to further improve green strength and green density. Warm compaction is a process in which both the die and the powder are heated to a modest temperature of ≈ 100 °C. In this process, heat is used to lower the yield point of metal particles, thereby facilitating deformation and increasing the compressibility of material. In the case of warm die compaction, only the die is heated and as such the temperatures achieved using this process are relatively lower. However, this process has been useful to decrease the lubricant content as it softens more quickly relative to conventional room temperature compaction. More recently, various additive manufacturing technologies that include material jetting, binder jetting, sheet lamination, direct energy deposition, and powder bed fusion have also been used to improve green density.[7] Particle size, shape, and distribution as well as binder composition are some of the material parameters that govern the density of the additive manufactured parts.

Recently, cold sintering process (CSP) has been developed to densify many ceramic materials and related composites at extremely low temperatures through the application of a deviatoric stress that couples with a transient chemical phase enabling dissolution and precipitation mechanisms. More than 100 different ceramics and composites have been densified using this approach at relatively modest temperatures <300 °C and compacting pressures ≈100 MPa.[8] The process has also been extended to demonstrate the effect in metals that are used to make electrodes in multilayer ceramic passive components such as varistors and capacitors, and microwave filters.[9] In addition, the low temperatures have enabled new types of nanocomposites with modified grain boundaries and confined interfacial polymers and nanomaterials. Cold sintering in these applications has also enabled cosintering of high-performance high conductivity inner electrodes of several metal chemistries with small particle sizes of ≈0.1 to 0.5 µm that include Ag, Cu, Ni, Fe, and Al. These metals under an applied stress can both cold sinter and densify under plastic deformation process to form the electrodes.[9] The term cold sintering in metals was previously introduced by Gutmanas et al. to the high-pressure compaction process of metals.[10] In this case, there was no transient chemical phases that enables the dissolution or precipitation phase but high stresses ≈4 GPa at room temperature enabled compaction and densification through plastic deformation. The ductile particulate materials such as Al, Cu, Co, Fe, and Fe–Ti alloys (316L, Inconel 600 and Ti_6AlV) as well as refractory metals such as Nb, Mo, Ta, and W were compacted using this process.[11]

In this investigation, we report cold sintering as a process utilizing particle surface modification followed by warm compaction of powders, which results in both improved densification and strengthening of compacts. The objective of this article is to provide insight on densification and microstructural evolution at the interface due to cold sintering mechanism. The high strength compacts promote green machining and can potentially open new processing route for the manufacture of soft magnetic iron composites.

2. Results and Discussion

Figure 1 shows the relative density of iron (control) and cold sintered compacts obtained at different pressures in the anisothermal region between room temperature and 200 °C. At room temperature ($t = 5$ s), the relative densities achieved for the control at compaction pressures of 70, 100, 200, and 700 MPa are 53.7%, 59.5%, 68.6%, and 92.7%, respectively. The relative density for the control does not drastically change when the temperature of the compact was raised gradually from room temperature to 200 °C. Curves of control samples at different pressures follow a similar pattern, as a small inflexion point is observed at approximatively $t = 250$ s. The slight increase in relative density observed after the inflexion point may be associated with a drop in the yield strength of iron upon heating.[13] The addition of phosphoric acid as a cold sintering aid consistently increases the relative densities of compacts at each pressure from $t = 60$ s (above 90 °C), up to 1–2% in the anisothermal region. In cold sintered samples, a systematic increase in relative density is observed after $t \approx 30$ s, likely due to chemical effects associated with the dissolution–precipitation creep mechanism.[14] At $t = 0$ s, the slight increase (<1%) in relative density observed between the control and the cold sintered samples for the 200–700 MPa pressure ranges may be due to enhanced particles rearrangement in the presence of a liquid phase.[15]

The impact of cold sintering aid on the green strength of the compacts is illustrated in **Figure 2**. Iron powders compacted at 620 MPa at room temperature had a typical green strength of 13 MPa, which is consistent with pressed powders using conventional P/M processes and acrawax binder. All the pressed samples had green density of ≈7.1–7.2 g cm^{-3} (91% relative density). When the powders were warm compacted at 100 °C, the green strength increased to about 30 MPa due to better interlocking between the particles. These values are comparable to high green strength of iron compacts achieved using specialty polymeric binders reported in the literature.[16b,c] The powders when treated with phosphoric acid and subjected to cold sintering conditions significantly improved the green strength to almost 65 MPa, which is more than two times that of the warm compacted control (Figure 2a). Systematic variation of phosphoric

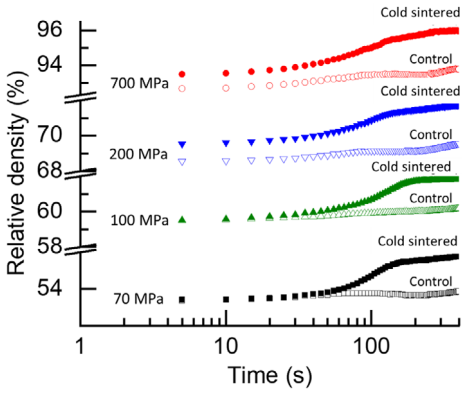

Figure 1. Evolution of the relative density of plain iron (control) and phosphoric acid-treated iron powders as a function of time when subjected to different pressures (70, 100, 200, and 700 MPa), at a constant heating rate in the anisothermal region.

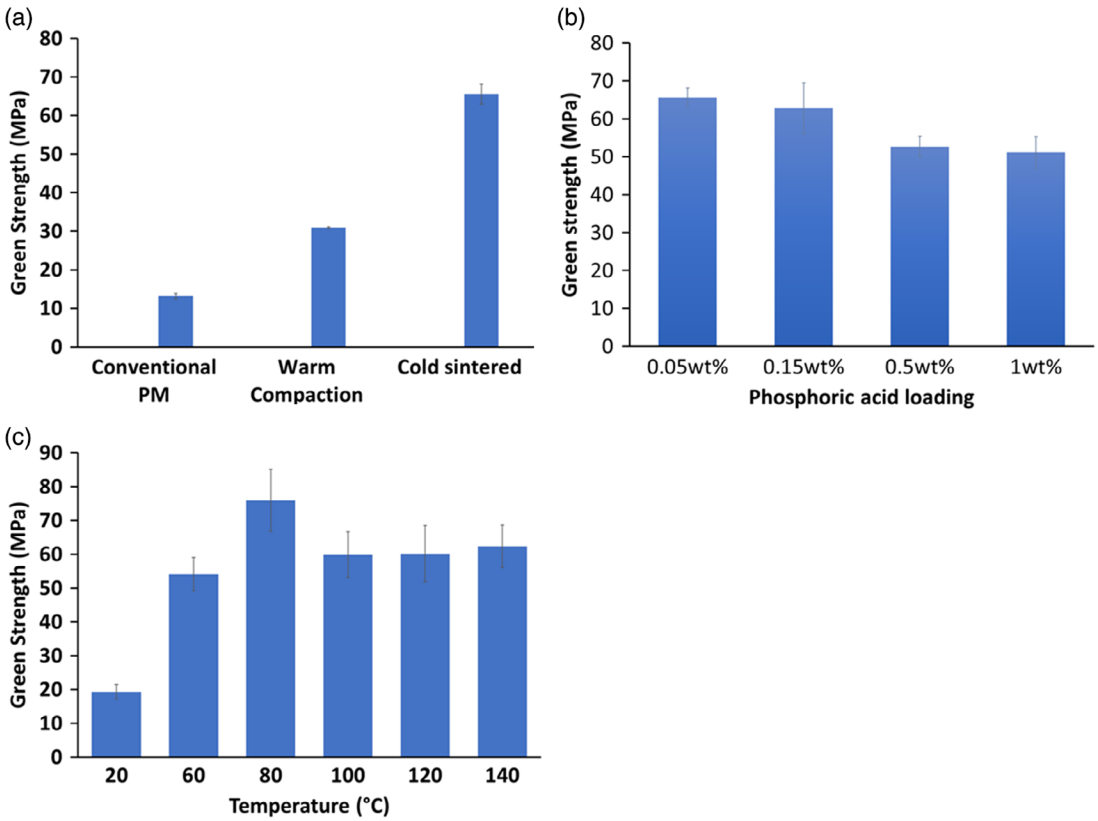

Figure 2. a) Comparison of green strength of iron compacts made using conventional PM, warm compaction, and cold sintering process; b) green strength as a function of phosphoric acid-treated powders made using different phosphoric acid loading and compacted at 620 MPa and 100 °C; and c) green strength as a function of compaction temperature of 0.15 wt% phosphoric acid-treated iron compacted at 620 MPa.

acid loading during surface modification showed that phosphoric acid loading as low as 0.05 wt% is enough to improve the green strength. Further increase in the phosphoric acid loading results in slight decrease in green strength as shown in Figure 2b. XRF analysis of the treated iron powders shows that the P content increased from 0.27 to ≈0.85 at% for 0.05 and 1 wt% phosphoric acid loading, respectively. Figure 2c shows the change in green strength of 0.15 wt% phosphoric acid loading with increased temperature. The treated powder when compacted at room temperature did not show any significant improvement relative to conventional P/M compacts. However, when the temperature was increased beyond 60 °C, there was considerable increase in the green strength, which remained relatively unchanged beyond 100 °C. The Hall flow rate of treated powders was ≈42 s which was similar to as-received iron powder (39 s), suggesting that the flow properties of the powders due to cold sintering chemistries were not significantly altered. This is very helpful in meeting the powder flow requirements in a manufacturing environment. Additionally, the fact that the green strength improved at a modest temperature of 60 °C suggests that it could also be extended to warm die compaction instead of warm compaction process.

Figure 3a,b shows the secondary electron and back scattered electron image of the fractured warm compacted control. The secondary electron image shows evidence of particles dislodging during the TRS measurement. The dark region in the backscattered image reveals the presence of binders at the particle interface. Intergranular fracture is the most dominant mode of failure in the control. Figure 3c,d shows the corresponding secondary electron and back scattered images of cold sintered sample. The secondary electron image shows much more denser compacts with several regions that indicate shearing of particles. The contrast under backscattered mode along with EDS mapping further accentuates these regions as seen from the white regions which represent sheared iron particles surrounded by phosphate coated iron. These features indicate that there is transgranular fracture in cold sintered sample and shows further evidence of strong cohesion between iron particles due to cold sintering.

TEM studies were done on carefully selected FIB cross sections of iron compacts that accounted for interfacial region between two iron particles. **Figure 4**a–c shows both the STEM and EDS mapped regions that capture the interface between two iron particles in warm compacted control. The STEM shows the presence of a 10 nm-thick iron oxide layer on the surface of both the particles. The presence of a small gap between the two particles is a clear indicator that physical interlocking is the primary contributor to the cohesive strength between the particles. EDS mapping shows the presence of Fe, O, and Mn near the particle interface. The base metal powder for iron is ATOMET 1001 which has 0.15% Mn. Figure 4d–f shows the TEM study

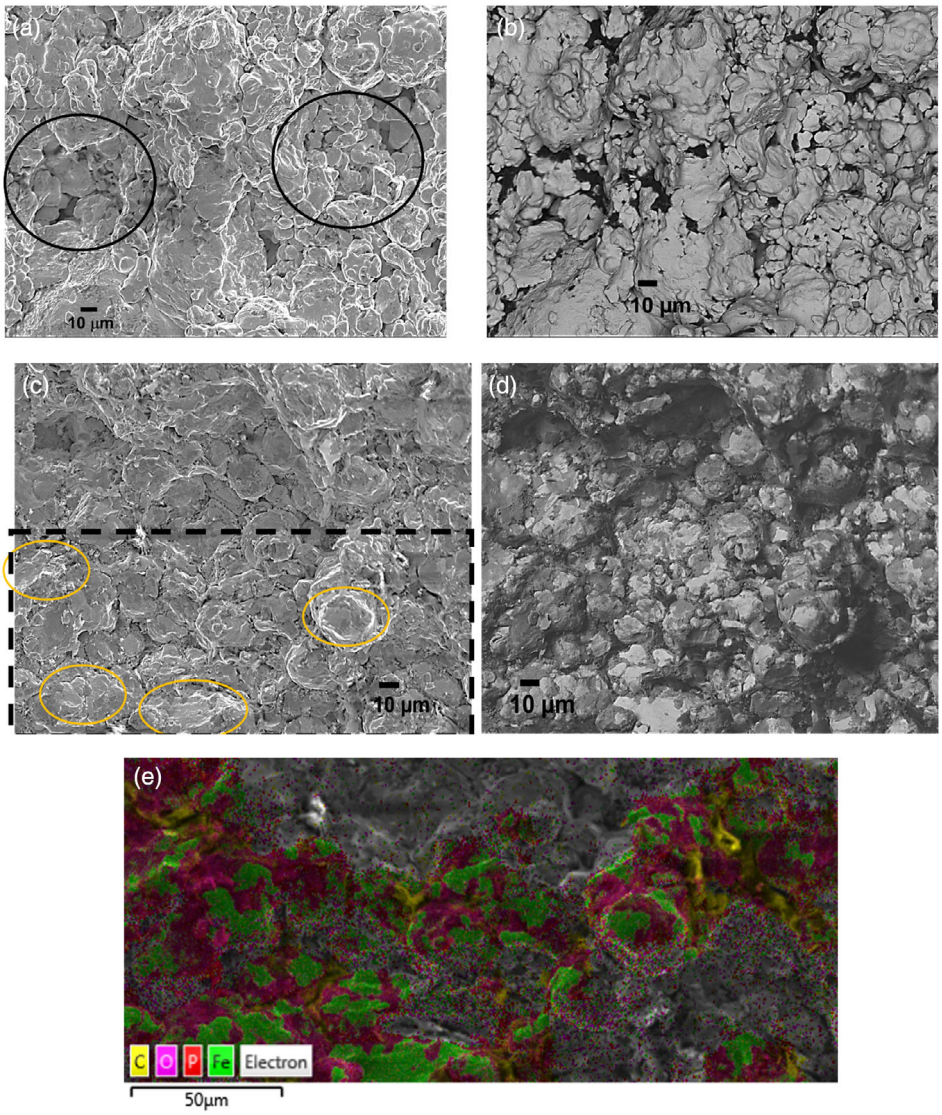

Figure 3. a) Cross-sectional secondary electron image of a fractured specimen made under warm compaction conditions (unmodified iron powder compacted at 100 °C); b) back scattered image of the fractured warm compacted iron sample; c) secondary electron image of fractured cold sintered iron compact made using phosphoric acid treated iron powder compacted at 100 °C; d) back scattered image of the fractured cold sintered iron compact; and e) EDS mapping showing elemental composition of selected area in part (c) of cold sintered iron compact.

on phosphate coated iron powder. We can see the presence of a continuous phosphate coating at the interfacial region between two iron particles. Unlike the control, this coating completely bridges the gap between the two Fe particles. Closer inspection of the interphase suggests that the coating is predominantly amorphous iron phosphate. However, there are also 1–2 nm dark nanocrystalline iron phosphate dispersed throughout the amorphous matrix. The iron phosphate interphase is ubiquitous across all particle interfaces, and we believe that this contributes primarily to the high cohesive strength of cold sintered iron compacts.

Figure 5 demonstrates the possibility of performing green machining on cold sintered iron compacts. The cold sintered compact in addition to providing sufficient mechanical stability to perform operations (facing, turning, and drilling) using milling machine and lathe can also be used for tapping. To our knowledge, this has not been demonstrated earlier and the results are quite extraordinary considering that the powdered sample has only been subjected to modest compaction temperatures and is devoid of any binder material.

The iron compacts were further subjected to conventional high-temperature sintering conditions in an industrial belt furnace. **Figure 6**a,b shows the etched microstructure of warm compacted control and cold sintered sample subjected to 1150 °C. The porosity between the grain boundaries in the warm compacted control can be clearly seen and is irregular in shape. On the other hand, cold sintered sample has relatively smaller well-rounded occluded porosity and larger grain growth that are characteristic of phosphorus containing sintered iron.[16] Previous studies on high-temperature sintering of phosphate-coated iron

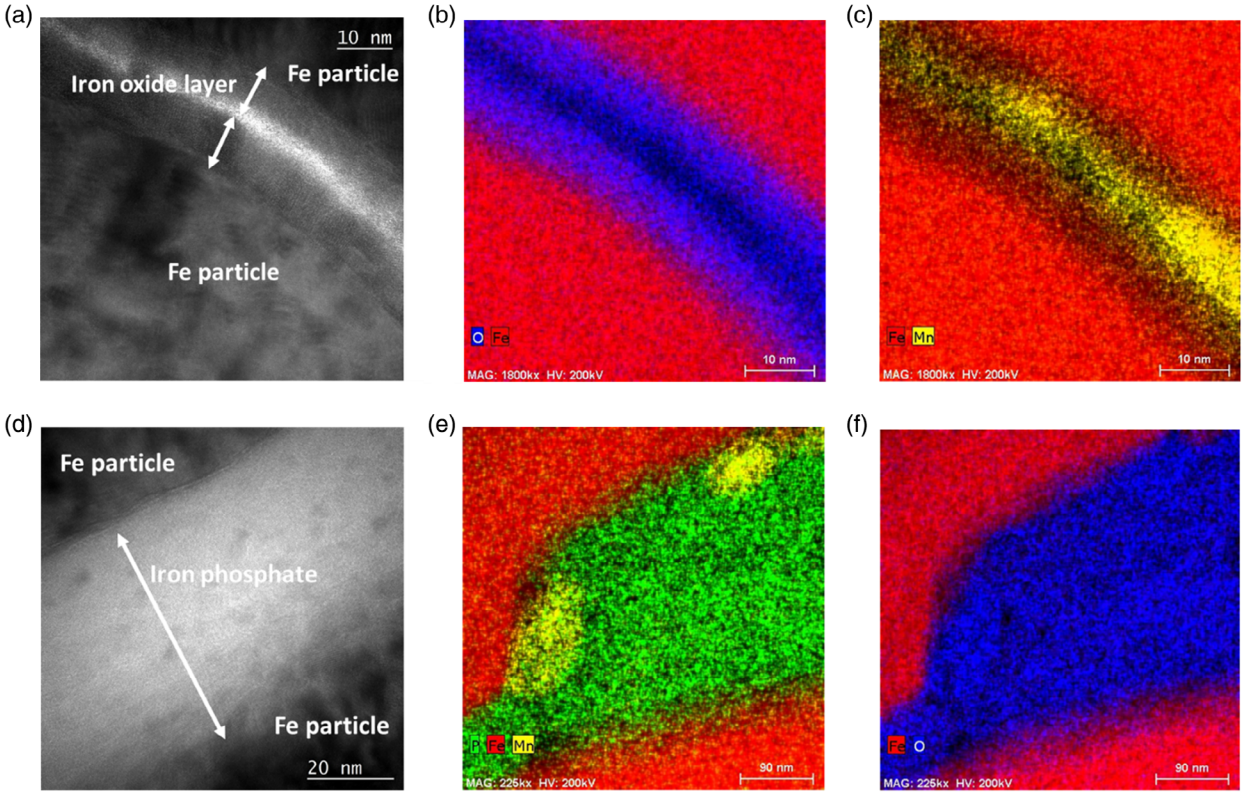

Figure 4. a) STEM micrograph of warm compacted iron (control), b,c) EDS mapping of warm compacted iron, d) STEM micrograph of cold sintered iron compact showing an iron phosphate interphase bridging two iron particles, and e,f) EDS mapping of cold sintered specimen interface.

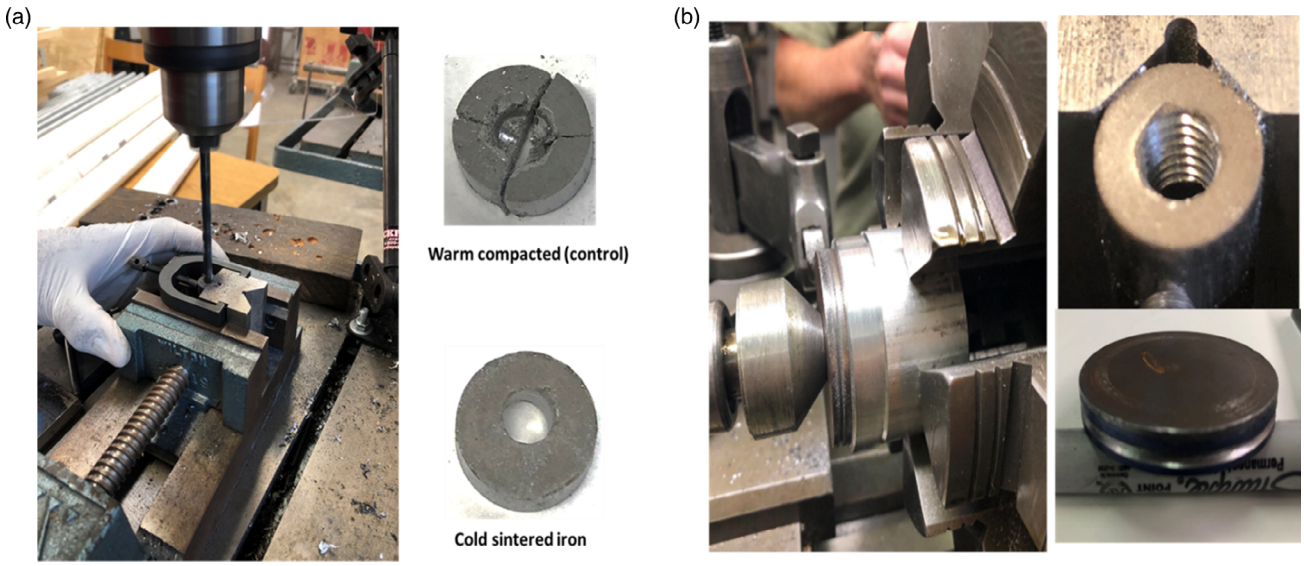

Figure 5. a) On the left, 0.5″ diameter cold sintered sample drilled using 0.25″ drill bit mounted on a milling machine; on the right, machinability of cold sintered sample relative to warm compacted iron (control) is demonstrated. b) On the left, 2″ diameter cold sintered sample mounted on a lathe and turning operation performed to create a groove in the compact (shown on the bottom right); on the upper right, a 0.5″ diameter cold sintered sample being tapped and threaded.

have shown that when the sintering temperature exceeds 1110 °C, there is a change in the microstructure due to liquid phase sintering that is created due to interactions in the Fe_2O_3–P_2O_5 system, leading to coarsening and joining of isolated iron particles to a continuous α-Fe phase surrounded by areas of solidified liquid phase, which is ferric phosphate compounds

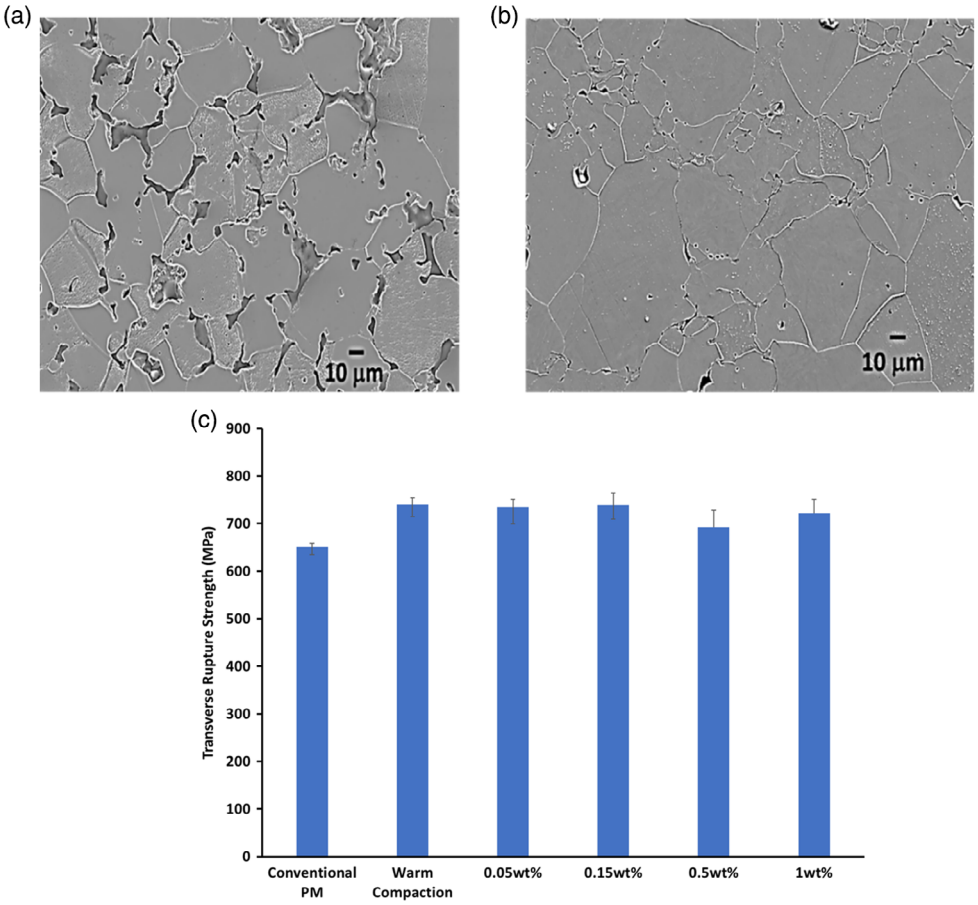

Figure 6. a) Scanning electron micrograph of etched warm compacted iron heat treated at 1150 °C under 90% N2 + 10% H_2 atmosphere; b) scanning electron micrograph of etched cold sintered sample heat treated at 1150 °C under 90% N_2 + 10% H_2 atmosphere; and c) comparison of transverse rupture strength of high-temperature sintered iron compacts made using room temperature conventional P/M process, warm compacted iron, and cold sintered samples made using varying amount of phosphoric acid.

such as $FePO_4$, Fe_3PO_7, $Fe_4(P_2O_7)_3$, and $Fe(PO_3)_3$.[17] Figure 6c shows the comparison of transverse rupture strength of control (conventional P/M at room temperature compaction and warm compaction) against the cold sintered sample. The transverse rupture strength of both warm compacted control and cold sintered samples was higher relative to conventional P/M at room temperature compaction.

The treated powders with various phosphoric acid loading up to 1 wt% showed relatively similar transverse rupture strength as shown in **Figure 7**b. However, the sintered density slightly decreased from 7.13 to 7.03 g cm^{-3} at 0.05 and 1 wt% phosphoric acid loading, respectively. Furthermore, bending tests were performed on high-temperature sintered warm compacted control and cold sintered circular (∅12.5 × 1.5 mm thick) specimens using an Instron universal testing machine. The convergence and flexural behavior of these specimens was also simulated using ANSYS finite element (FE) software and validated by comparing the results with experimental values as shown in **Figure 8**. The FE modeling was performed using augmented Lagrange formulation with frictional contacts between mating surface and large deflection analysis. Material and geometrical nonlinearities were considered in the analysis, and both force and displacement tolerance convergence values were set to 0.001. In order to fit the load–deflection curves for both the samples, the material properties of sintered iron-based P/M parts were used in the ANSYS model for the control sample and modified for the reduced porosity in the cold sintered specimen.[18] It is clear from Figure 7 that the numerical and experimental results were comparable and showed that there was appreciable improvement in both elastic modulus and yield strength of cold sintered sample after high-temperature treatment. The elastic modulus and yield strength increased from 100 to 160 GPa and 100 to 150 MPa, respectively, while the tangential modulus decreased from 1.45 to 1.2 GPa.

In order to gain insight on the structural change during CSP, in situ DRIFTS experiment was conducted on the treated powders. The DRIFTS spectra were collected as a function of temperature with the temperature ranging from 22 to 200 °C as shown in Figure 8. The spectrum collected at room temperature showed distinct peaks characteristic of hydrated phosphates with a broad peak at 3200–3500 cm^{-1} corresponding to −OH stretch and a peak at 1640 cm^{-1} related to H_2O bending mode. The intensity of both peaks decreased with increase in temperature indicative of elimination of water under cold sintering conditions.

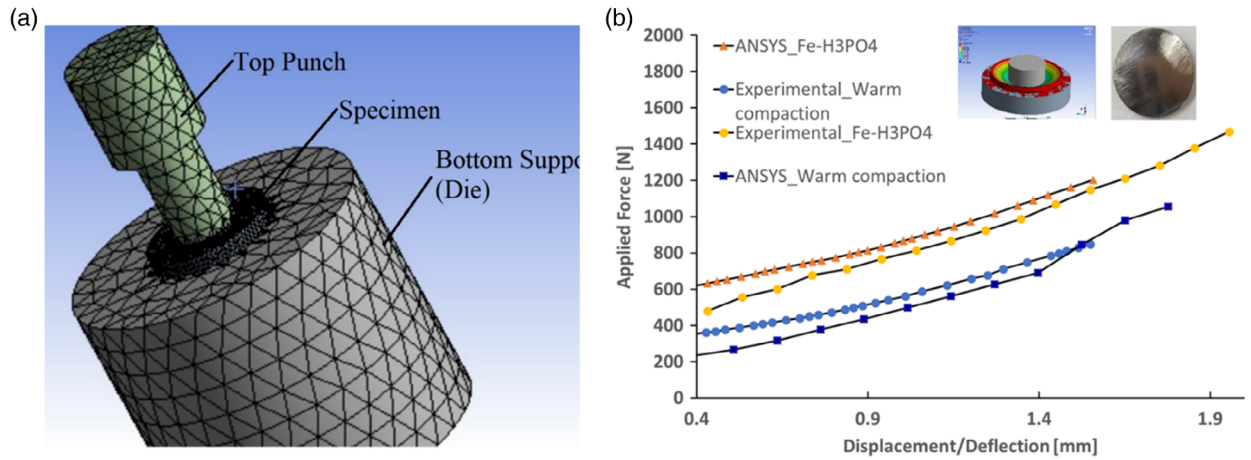

Figure 7. a) Meshing of top punch, sample, and bottom support using ANSYS for modeling the performance of circular bending test and b) force–deflection curve of high-temperature sintered warm compacted iron (control) and cold sintered sample fitted using ANSYS.

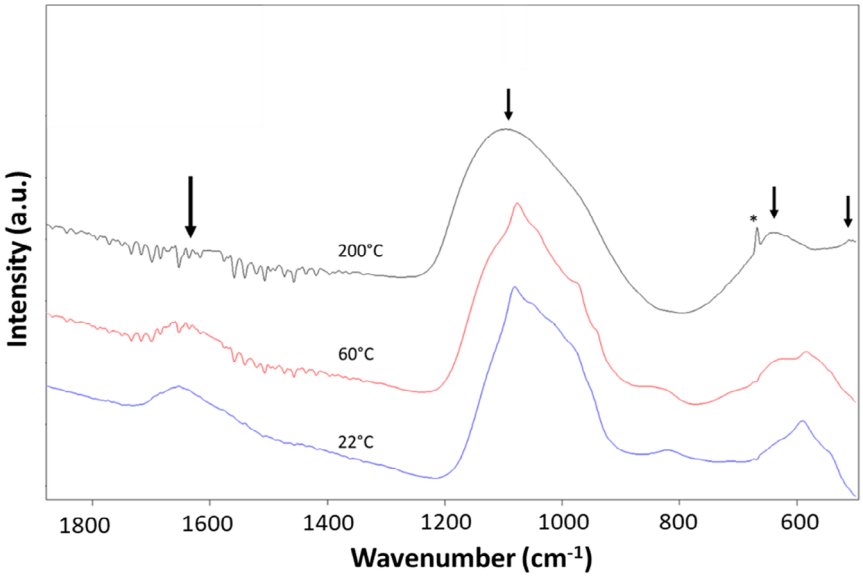

Figure 8. DRIFTS spectra of phosphoric acid-treated iron powder as a function of temperature. *An artifact peak due to presence of CO_2 gas in air.

The presence of P–O and P–O–P linkage was seen from the presence of multiple peaks in the range of 900–1200 cm^{-1} and 500–800 cm^{-1}, respectively.[19] Phosphates can be formed as isolated tetrahedron (PO_4^{3-}) denoted as Q^0, two phosphate tetrahedra connected by a bridging oxygen ($P_2O_7^{4-}$) denoted as Q^1, or a higher ordered chain connecting phosphate tetrahedra with two bridging oxygens ($P_3O_{10}^{5-}$) denoted as Q^2, respectively.[20] At room temperature and 60 °C, we see a sharp peak at 1080 cm^{-1} which gets upshifted and becomes broader at 200 °C. The peak at 1080 cm^{-1} is attributed to the presence of Q^1 units and an upshift may be indicative of forming higher order Q^2 units. Additionally, the gradual disappearance of shoulder peak at 980 cm^{-1} with the emergence of a peak around 630 and 500 cm^{-1} is also indicative of the formation of Q^2 units at the expense of Q^0 and Q^1 units at 200 °C. We anticipate that these changes could be further accelerated by the application of pressure under cold sintering conditions. Our results indicate that under cold sintering conditions, two things occur. First, there is increased mobility and transport of water phase at the interface which acts as the transient liquid phase promoting rearrangement, dissolution, and precipitation at the particle boundary. Second, the structure of orthophosphates and pyrophosphates may be converted into higher order polyphosphates and the resultant stronger covalent P–O–P linkages increases the cohesive strength at the particle interfaces. **Table 1** summarizes various infrared bands and their assigned peaks.

It is also remarkable to see distinct microstructural change under cold sintering conditions as shown in **Figure 9**. We notice that the warm compacted control has many interconnected pores while the pores in the cold sintered compacts are relatively less and far more isolated. Additionally, we also see the presence of several triple junction points that clearly show solid–solid

Table 1. Infrared peak positions and their corresponding band assignments of hydrated phosphate functional groups.

Peak position [cm^{-1}]	Band assignment
3200–3500	−OH stretch
1640	H_2O bending mode
1100–1130	Symmetric stretching vibration of P—O bonds in Q^2 units
1080	Asymmetric stretching vibrations of P—O bonds [Q^1 units]
980–990	Asymmetric stretching of P—O bonds [Q^0 units]
830	Asymmetric stretching vibration of P–O–P [Q^0 units]
630	Asymmetric stretching vibration of P–O–P [Q^2 units]
500	Asymmetric bending vibrations of P—O bonds [Q^2 units]

interfaces. Liu et al. had developed a strength model that describes the major driving force for densification during liquid phase sintering in terms of capillary force and solid bonding effect.[21] They state that during the initial stages, capillary forces aid in the rearrangement and densification via viscous flow. But as the compacts form a percolated structure, the rigidity of the compact is primarily influenced by solid bonding between the particles. Contiguity, which is a quantitative measure of the interphase contact (ratio of contact area to grain surface area), takes into account both these factors. The model describes the driving force capillary force pressure as

$$P_n = \frac{5.2\ \gamma_{LV}\cos\theta}{D(\Delta L/L_0)} \tag{1}$$

where the value of $\Delta L/L_0$is obtained from the dilatometry experiment, average particle size, D, of ≈100 μm was used based on laser diffraction data, γ_{LV} for water is 5.89×10^{-2} MPa at 100 °C, and we assume incipient wetting at the interface.

Under cold sintering conditions, as we apply both pressure and temperature, we also include stress due to plastic deformation in the compact strength equation as follows

$$\sigma = \frac{3V_s}{2}(P_n + \sigma_0 C_{ss}) + \sigma_w \tag{2}$$

where V_s is the solid volume fraction, σ_0 is the yield strength of iron, C_{ss} is the contiguity factor, and σ_w is the stress due to plastic deformation during compaction. σ_w was computed based on the compact strength of room temperature P/M compacts, which is devoid of capillary driving force and solid–solid bonding.

Figure 10 shows the relationship between compact strength and contiguity factor, C_{ss}, as predicted by the model. The compact green strength as determined by TRS measurements is represented in the plot and based on the model, contiguity factor is determined. The model defines a critical contiguity for no distortion based on percolation theory as 0.38 as

$$\sigma = \begin{cases} \frac{3}{2}V_s\sigma_0 C_{ss} + \sigma_w & \text{for } C_{ss} > 0.38 \\ \sigma_w & \text{for } C_{ss} < 0.38 \end{cases} \tag{3}$$

As shown in the plot, the contiguity factor for both the controls (room temperature compaction and warm compaction) is below the contiguity factor as the primary contribution to both these samples was plastic deformation aided mechanical interlocking of particles. All the cold sintered samples prepared under varying conditions showed contiguity factor ranging from 0.55 to 0.76, which is significantly greater than the critical contiguity factor. These higher numbers indicate that the contribution from solid–solid bonding is greater, and the chemical bonding as evidenced from DRIFTS experiment during cold sintering plays an

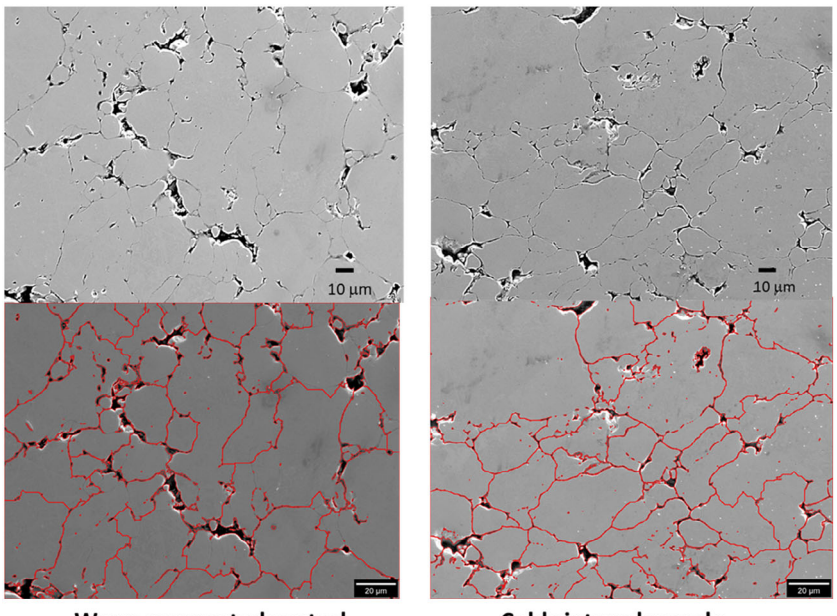

Figure 9. Comparison of microstructure of warm compacted control and cold sintered sample compacted at 620 MPa and 100 °C. Image analysis showing the particle boundary and highlighting the presence of porosity and triple junction in the compacted samples.

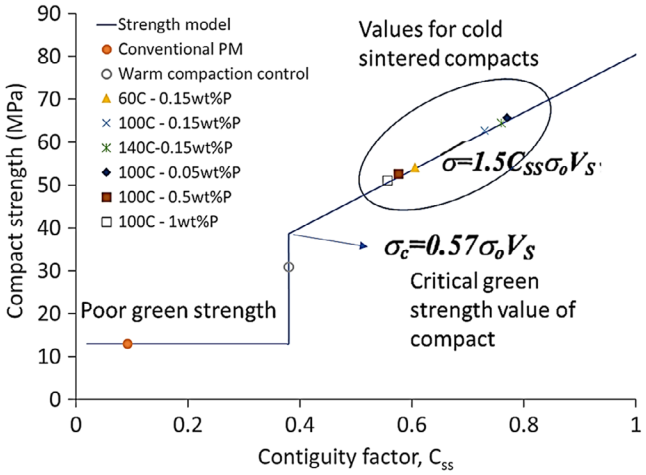

Figure 10. Strength model showing the increase in contiguity factor for cold sintered specimen relative to warm compaction and conventional PM control samples.

important role. German et al. have also described a model that shows the contiguity variation with dihedral angle and solid volume fraction as[22]

$$C_{ss} = V_s^2(0.43\sin\phi + 0.35\ \sin^2\phi) \quad (4)$$

The equation was developed to describe spherical particles and as such cannot be directly applied to the irregular shaped iron particles in this work. However, it is clear from the equation that for a similar solid volume fraction, increase in contiguity factor will result in corresponding increase in the dihedral angle. This trend was validated by the good agreement of apparent 2D dihedral angles measured based on the microstructure of warm compacted control and cold sintered samples as shown in **Figure 11**. The dihedral angle distribution of warm compacted control ranges between 30° and 60° with very few triple junctions as denoted by a dihedral angle of 120°. On the other hand, cold sintered samples show an upshift with dihedral angles ranging from 50° to 90° along with the presence of significant number of triple junctions.

The article thus describes the development of a low-temperature transient liquid sintering process called cold sintering that helps to significantly increase the green strength of powdered metal compacts. Elimination of water from a thin layer of hydrated phosphate layer around iron particles forms the liquid phase and provides the impetus to initiate rearrangement and densification of compact during cold sintering. Simultaneously, we also see evidence for strong solid–solid bonding at interface due to the structural transformation of phosphate to form chain or polyphosphates with covalent P–O–P linkages that forms a co-continuous phase at the particle interfaces as shown in **Figure 12**. The use of pretreated iron powders limits the phosphorus content on iron to less than 1 at% and as such when subjected to high-temperature treatment, it does not result in deterioration of the mechanical properties as demonstrated by both the TRS and circular bending measurements.

With cold sintering, there are potential opportunities to extend the process across many alloy systems with the basic process and strategies identified from this model iron demonstration. In addition, working at these low temperatures and enhanced strengths along with the machining opportunities can help in increasing manufacturing production rates, as compositions that are more readily machined can be shaped and later resintered to design with appropriate hardness with a time–temperature–transformation strategy. In addition, new types of composites could be noted with this processing strategy with different alloyed metal powders, cermets, and beyond to design functional properties in P/M. It also opens pathways to design insulating boundaries at iron particle interface and fabricate soft magnetic composites, which is a critical application targeted by P/M industries to aid the electrification of automotive market.[23]

3. Conclusions

Cold sintering is a low-temperature densification process that has been demonstrated widely in various ceramic materials. We adopt this process to improve the densification and strengthening of powdered metal iron compacts. This has been achieved by first modifying the surface of iron using a hydrated phosphate layer prior to the warm compaction. During warm compaction, H_2O molecules resulting from the phosphate coating dehydration acts as a transient liquid phase promoting densification

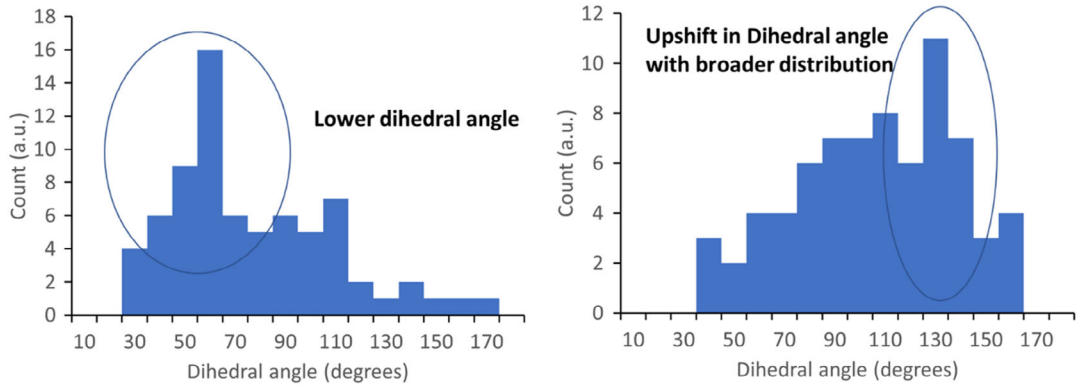

Figure 11. 2D dihedral angle measurements based on the microstructure of warm compaction control and cold sintered sample.

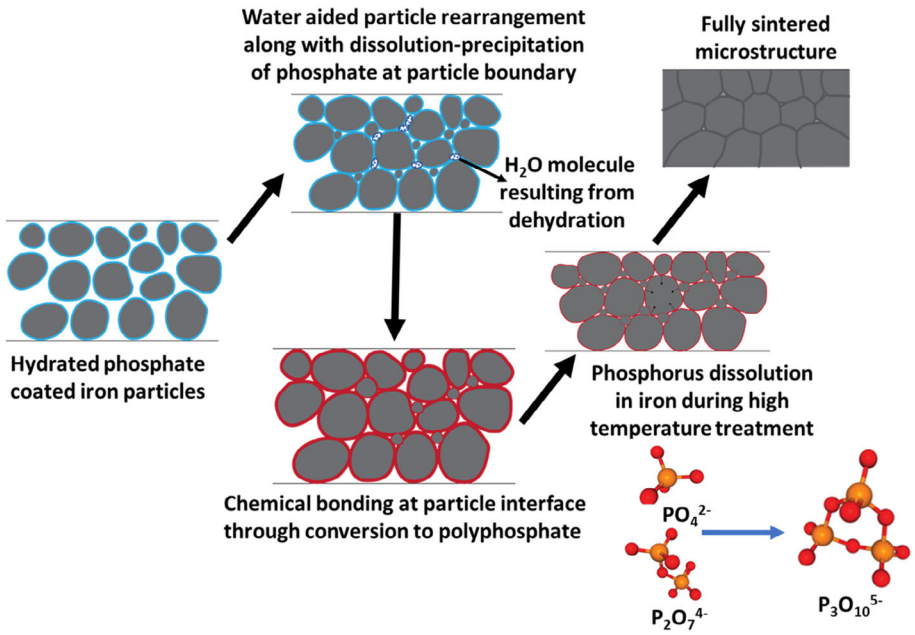

Figure 12. Schematic illustrating the impact of CSP on densification and strengthening of powdered iron compact.

through rearrangement and dissolution–precipitation processes at particle interfaces. The interfacial solid–solid bonding is further strengthened by the chemical transformation of phosphates and pyrophosphates to polyphosphates. The impact of cold sintering on densification was demonstrated using dilatometry studies while the improved green strength measured using transverse rupture strength analysis showed that the process can facilitate green machining. A strength model based on microstructural analysis suggests that cold sintering results in stronger bonding at the interface. Proper choice of cold sintering chemistries and the associated chemomechanical processes at the particle contact can potentially provide a generic solution to improving green strength and green density of powdered metal compacts used in P/M industries. Furthermore, with these improvements it opens new opportunities to manufacturing strategies for higher performance components.

4. Experimental Section

Iron powder (ATOMET 1001) for the study was provided by Advantage Powdered Metals Inc. A known amount of phosphoric acid (ranging from 0.05 to 1 wt%) relative to the mass of iron powders was dissolved in 500 mL of water. Iron powder (250 g) was treated by mixing the powder in the aqueous phosphoric acid solution for 10 min. The resultant mixture was then filtered, washed thoroughly with ethanol, and dried at room temperature. The as-treated powder was then mixed with Acrawax binder (0.75 wt%) in a turbula for 30 min prior to cold sintering.

In order to prepare the transverse rupture strength (TRS) bars (according to MPIF Standard 41), the treated powders were first heated in a hot die placed in a Carver hot press until the temperature of the powder was the same as the die. TRS samples were then made at a compaction pressure of 620 MPa for 10 s. The cold sintering conditions were varied by changing the processing temperature from room temperature to 100 °C. Two controls produced for the study were conventionally compacted at room temperature (no surface treatment or heating) and warm compacted (with no surface treatment), respectively. The samples were compacted using the as-received iron powders using the same die and pressure as cold sintered samples. Additionally, a 0.5″ and 2″ diameter hot dies were used to prepare samples that were ≈0.25″ thick to perform green machining operations. The green machining operations were demonstrated on cold sintered samples that had no binder. Some cold sintered TRS bars were then subjected to high-temperature sintering conditions using an industrial belt furnace maintained at 1150 °C under 90% nitrogen + 10% hydrogen atmosphere at a belt speed of 0.15 m min^{-1} (≈6 in min^{-1}). The samples were subject to high-temperature sintering in the belt furnace for 30 min.

The densification behavior of both the iron powder (control) and the phosphoric acid treated iron powder was investigated using an apparatus that has 1) an ENERPAC press in constant pressure mode, thanks to an electric hydraulic pump and 2) a dilatometer equipped with a Keyence GT2-H32 Digital Contact Sensor.[12] In our study, both the control and the modified powders were first compacted at room temperatures at different pressures: 70, 100, 200, and 700 MPa for 10 s. For each given pressure, dilatometry data were collected in the anisothermal region, between room temperature and 200 °C using a 22.5 °C min^{-1} average heating rate.

The axial displacement measured during CSP was corrected to account for the thermal expansion of the die, piston, and punches. The calculated time-dependent thickness evolution ($L(t)$) was converted to relative density profiles using sample mass (m), area (A), and theoretical density (ρ_{th}) of iron powder as follows

$$\rho_{rel}(t) = \frac{m}{AL(t)\rho_{th}} \tag{5}$$

The relative densities as a function of densification time at different pressures were then compared for both the control and cold sintered compacts.

The morphology of fractured cold sintered compacts and controls as well as microstructural characterization of high-temperature sintered samples were studied using JEOL JSM-7200F FESEM microscope. The high-temperature sintered samples were sectioned, mounted, polished, and etched in Nital solution (2%) to reveal the grain boundaries. Image analyses were performed using MIPAR and ImageJ software. Transmission electron microscopy for high-resolution microstructural analysis was

measured at 200 kV (TALOS F200X, FEI). The samples for the analysis were prepared using focused ion beam (FIB) system (Helios 660, FEI). Scanning transmission electron microscopy–energy dispersive X-ray spectroscopy (STEM-EDS) was measured using STEM with SuperX EDS system (TALOS F200X, FEI) for elemental mapping. Additionally, X-ray fluorescence (XRF) analysis was performed using Epsilon XRF instrument to measure the phosphorus content of the treated powders. DRIFTS analysis was performed using FT-IR Bruker V70 instrument to study the chemical structure of phosphate coating on iron particles. DRIFTS cell was used to perform in situ experiments under argon atmosphere at various temperatures ranging from 22 to 200 °C, respectively. Tranverse rupture strength was measured by mounting the sample on a three-point bending fixture and applying load using an Instron universal testing machine.

Acknowledgements

The authors would like to thank PA Manufacturing Innovation program, Department of Community and Economic Development: Powdered Metal Initiative, Appalachian Regional Commission (ARC) grant from Clearfield County and Penn State Commonwealth campus innovation fund for providing financial support for the project. C.R. would also like to thank NSF FMSG (2134643) and AFOSR (FA 9550-19-1 0372) for partial support of this work. The authors would also like to thank the Materials Characterization Laboratory (MCL) at University Park for providing access to state-of-the-art characterization facilities.

Conflict of Interest

The authors declare no conflict of interest.

Data Availability Statement

The data that support the findings of this study are available from the corresponding author upon reasonable request.

Keywords

cold sintering, green machining, green strength, powder metallurgy, warm compaction

Received: May 17, 2022
Revised: June 26, 2022
Published online: July 20, 2022

[1] H. Kulkarni, V. V. Dabhade, *J. Manuf. Process.* **2019**, *44*, 1.
[2] E. Klar, W. M. Shafer, *Metall. Trans. A* **1976**, *7*, 1470.
[3] M. Kejzelman, P. Skoglund, O. Andersson, P. Knutsson, H. Vidarsson, B. Skarman, US20040191519A1, **2004**.
[4] a) D. S. Coleman, J. N. Foba, *Powder Metall.* **1989**, *32*, 35; b) L. P. Lefebvre, Y. M. Henuset, Y. Deslandes, G. Pleizier, *Powder Metall.* **1999**, *42*, 325.
[5] a) P. J. James, *Powder Metall.* **1977**, *20*, 21; b) J. A. Lund, *Int. J. Powder Metall.* **1982**, *18*, 117.
[6] a) M. Gauthier, L. P. Lefebvre, Y. Thomas, M. N. Bureau, *Mater. Manuf. Process.* **2004**, *19*, 793; b) L. Tremblay, Y. Thomas, *Adv. Powder Metall. Particul. Mater.* **1999**, *1*, 141; c) S. H. Luk, A. B. Davala, *Adv. Powder Metall. Particul. Mater.* **1996**, *5*, 127.
[7] a) M. Li, W. C. Du, A. Elwany, Z. J. Pei, C. Ma, *J. Manuf. Sci. E-T Asme.* **2020**, 142; b) N. Tuncer, A. Bose, *JOM* **2020**, *72*, 3090; c) V. V. Popov, M. L. Grilli, A. Koptyug, L. Jaworska, A. Katz-Demyanetz, D. Klobcar, S. Balos, B. O. Postolnyi, S. Goel, *Materials* **2021**, 14; d) J. Gonzalez-Gutierrez, S. Cano, S. Schuschnigg, C. Kukla, J. Sapkota, C. Holzer, *Materials* **2018**, 11; e) Y. Zhang, L. M. Wu, X. Y. Guo, S. Kane, Y. F. Deng, Y. G. Jung, J. H. Lee, J. Zhang, *J. Mater. Eng. Perform.* **2018**, *27*, 1.
[8] a) S. S. Berbano, J. Guo, H. Z. Guo, M. T. Lanagan, C. A. Randall, *J. Am. Ceram. Soc.* **2017**, *100*, 2123; b) J. H. Seo, J. Guo, H. Z. Guo, K. Verlinde, D. S. B. Heidary, R. Rajagopalan, C. A. Randall, *Ceram. Int.* **2017**, *43*, 15370; c) J. H. Seo, K. Verlinde, J. Guo, D. S. B. Heidary, R. Rajagopalan, T. E. Mallouk, C. A. Randall, *Scr. Mater.* **2018**, *146*, 267; d) H. Z. Guo, A. Baker, J. Guo, C. A. Randall, *ACS Nano.* **2016**, *10*, 10606; e) H. Z. Guo, A. Baker, J. Guo, C. A. Randall, *J. Am. Ceram. Soc.* **2016**, *99*, 3489; f) H. Z. Guo, J. Guo, A. Baker, C. A. Randall, *Acs Appl. Mater. Interf.* **2016**, *8*, 34170; g) J. Guo, S. S. Berbano, H. Z. Guo, A. L. Baker, M. T. Lanagan, C. A. Randall, *Adv. Funct. Mater.* **2016**, *26*, 7115; h) J. Guo, H. Z. Guo, A. L. Baker, M. T. Lanagan, E. R. Kupp, G. L. Messing, C. A. Randall, *Angew. Chem.-Int. Ed.* **2016**, *55*, 11457; i) S. Funahashi, J. Guo, H. Z. Guo, K. Wang, A. L. Baker, K. Shiratsuyu, C. A. Randall, *J. Am. Ceram. Soc.* **2017**, *100*, 546; j) A. Baker, H. Z. Guo, J. Guo, C. Randall, *J. Am. Ceram. Soc.* **2016**, *99*, 3202.
[9] T. H. de Beauvoir, S. Dursun, L. S. Gao, C. Randall, *Acs Appl. Electron. Ma.* **2019**, *1*, 1198.
[10] E. Y. Gutmanas, A. Rabinkin, M. Roitberg, *Scr. Metall.* **1979**, *13*, 11.
[11] a) E. Y. Gutmanas, *Powder Metall. Int.* **1980**, *12*, 178; b) E. Y. Gutmanas, A. Rabinkin, M. Roitberg, *Mater. Sci. Eng.* **1980**, *45*, 269; c) D. B. Goldman, E. Y. Gutmanas, *Powder Metall. Int.* **1985**, *17*, 269; d) D. B. Goldman, E. Y. Gutmanas, D. Zak, *J. Mater. Sci. Lett.* **1985**, *4*, 1208; e) E. Y. Gutmanas, D. B. Goldman, S. Hart, D. Zak, *Powder Metall. Int.* **1986**, *18*, 401.
[12] R. Floyd, S. Lowum, J. P. Maria, *Rev. Sci. Instrum.* **2019**, *90*.
[13] G. F. Bocchini, *Powder Metall.* **1999**, *42*, 171.
[14] S. A. Ndayishimiye, M. Y. Sengul, T. Sada, T. Sada, S. Dursun, S. H. Bang, Z. G. Grady, K. Tsuji, S. Funahashi, A. C. T. Van Duin, C. A. Randall, *Open Ceramics* **2020**, *2*, 100019.
[15] J. Klein, *Masters, Department of Mechanical Engineering, University of California*, Berkeley **1975**.
[16] A. Muthuchamy, R. Kumar, A. R. Annamalai, D. K. Agrawal, A. Upadhyaya, *Mater. Character.* **2016**, *114*, 122.
[17] M. Kabatova, E. Dudrova, H. Brunckova, *Surf. Interface Anal.* **2013**, *45*, 1166.
[18] A. V. Manoylov, F. M. Borodich, H. P. Evans, in *Proc. Roy. Soc. A-Math. Phys. Eng. Sci.* **2013**, *469*, 20120689.
[19] M. Q. Shi, Y. J. Liang, L. Y. Chai, X. B. Min, Z. W. Zhao, S. Yang, *J. Mol. Struct.* **2015**, *1081*, 389.
[20] P. Stoch, A. Stoch, M. Ciecinska, I. Krakowiak, M. Sitarz, *J. Non-Cryst. Solids* **2016**, *450*, 48.
[21] J. X. Liu, R. M. German, *Metall. Mater. Trans. A* **1999**, *30*, 3211.
[22] R. German, P. Suri, S. Park, *J. Mater. Sci.* **2009**, *44*, 1.
[23] R. Ramakrishnan, C. Randall, S. Nayir, D. Waryoba, 62/907, 950, **2019**.